Design, Development, and Testing of a Shrouded Single-Rotor Micro Air Vehicle with Antitorque Vanes

Vikram Hrishikeshavan*
Graduate Research Assistant
Alfred Gessow Rotorcraft Center
University of Maryland
College Park, MD

Jayant Sirohi
Assistant Professor
Aerospace and Mechanical Engineering Department
University of Texas, Austin, TX

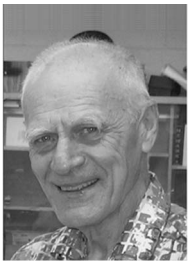

Marat Tishchenko
Visiting Professor

Inderjit Chopra
Alfred Gessow Professor and Director
Alfred Gessow Rotorcraft Center, University of Maryland
College Park, MD

Rotary-wing micro air vehicles (MAVs) operate at low Reynolds number flows and have poor hover aerodynamic efficiency. In this paper, the design and testing of a shrouded single-rotor MAV for improved hover efficiency and payload capability is described. The vehicle consists of a single fixed-pitch, two-bladed rotor with axisymmetric vanes placed in the rotor downwash to counter the rotor torque and improve vehicle compactness. Comparison in hover performance of the two-bladed rotor with and without the shroud indicated that the shrouded rotor had a 40% improvement in power loading and a payload benefit of up to 11% of the vehicle weight after taking the weight of the shroud into consideration. A hingeless rotor was found to be suitable for incorporation in the shroud. To eliminate possible cross-coupling in pitch and roll, the Hiller bar was suitably phased with respect to blade pitching axis. The final shrouded rotor vehicle was built weighing 257 g. It was flown in hover demonstrating good maneuverability. The feasibility of improved power loading of a rotary-wing MAV through the shrouded rotor concept was successfully demonstrated.

Nomenclature

A	rotor disk area
C_{l_α}	airfoil lift curve slope, 1/deg
C_T	rotor thrust coefficient, $T/\rho A(\Omega R)^2$
C_T/σ	blade loading
c	airfoil chord, mm
c_d	airfoil drag coefficient
c_l	airfoil lift coefficient
D_t	shroud throat diameter
R	radius
Re	Reynolds number
t	airfoil thickness, mm
γ_R	rotor Lock number
η	motor efficiency
θ_V	angle of incidence of vane chord with respect to rotor axis, deg
θ_{Swirl}	change in angle of attack of rotor downwash due to swirl effects, deg
κ	induced power correction factor
ν_β	nondimensional blade rotating natural flap frequency
ρ	air density
σ	rotor solidity
σ_d	diffuser expansion ratio
$\mathbf{\Omega}$	rotor rotation speed, rad/s

*Corresponding author; email: vikramh@umd.edu.
Manuscript received September 2009; accepted August 2010.

Introduction

Micro aerial vehicles (MAVs) have received considerable interest over the past decade. They can be used to perform a variety of tasks that may be hazardous for manned vehicles, in both the military and civilian sectors. Some of the MAV missions include indoor and outdoor surveillance, covert imaging, urban intelligence gathering, and biological and chemical agent detection. Many of these missions require the MAVs to loiter for long periods of time as well as have the capability to operate in confined areas. Such tasks can be realized through efficient maneuverable rotary-wing MAVs.

Owing to their small size, rotary-wing MAVs operate at low Reynolds numbers where viscous effects are predominant. These result in a high profile drag, and as a result, lower aerodynamic efficiency compared to conventional full-scale vehicles. Hence, it is important to improve power loading of MAVs by adopting simple passive schemes without compromising greatly on vehicle weight. Therefore, the focus of this paper is the design, development, and testing of a rotary-wing MAV that utilizes the shrouded rotor concept.

The shroud minimizes rotor tip losses and produces extra thrust developed on the shroud inlet surface (Refs. 1, 2). It also serves to protect the rotor from its surroundings, which is a major advantage, especially in indoor applications. Because of these advantages, there have been several shrouded fan vehicles developed, such as the Cypher (Ref. 3), T-Hawk (Ref. 4), iSTAR (Ref. 5), GTSpy (Ref. 6), and TiShrov (Table 1). TiShrov, discussed in this paper, is the smallest entry in this field of vehicles. It is primarily designed for hover to low-speed

DOI: 10.4050/JAHS.56.012008

Table 1. Existing shrouded rotor vehicles

Vehicle	GTOW[a] (kg)	Rotor System, Lateral and Yaw Control	Rotor Diameter (m)	Thrust/Installed Power (N/W)	Disk Loading (N/m^2)
Cypher	200	Coaxial, variable pitch prop, swashplate (lateral), vanes (yaw)	1.1	0.053	2,062
iSTAR	1.4	Single, fixed pitch prop, fully deflectable vanes (lateral and yaw)	0.23	0.015	340
RQ-16 MAV	7.7	Single, fixed pitch prop, fully deflectable vanes (lateral and yaw)	0.33	0.025	882
TiShrov	0.26	Single, fixed pitch rotor, swashplate (lateral), partially deflectable vanes (yaw)	0.25	0.042	52

[a]GTOW, Gross takeoff weight.

Table 2. Vehicle prototypes tested

Prototype	Description
TiFlyer	Unshrouded, teetering rotor with vanes. Metal body construction. Mass: 350 g
Giant	Unshrouded, teetering rotor with vanes. Carbon fiber structure. Mass: 237 g
TiShrov	Shrouded, hingeless rotor with vanes. Carbon fiber structure. Mass: 257 g

forward-flight applications. To improve the compactness of the vehicle, the antitorque system was designed with vanes installed in the downwash of a single main rotor. This concept was first proposed by Nagler and Hafner (Ref. 7). Several vehicles (Refs. 3–6) have been developed with this configuration. However, the effects of the vanes on hovering efficiency, yaw authority, and ground effect have not been reported in the literature.

Based on the above discussion, it is envisioned that a good hover-efficient, maneuverable MAV may be developed with the shrouded rotor concept in conjunction with antitorque vanes. A conceptual design of the vehicle was generated, based on the mission requirements (Fig. 1). Bench-top experiments were performed to investigate key aspects of the design such as the antitorque mechanism and the effect of vanes and shroud on power loading. The main goals of the design include increased hover endurance, payload, and robustness. Based on the results of the performance tests, a series of risk reduction prototypes were built (Table 2). The first prototype with an unshrouded teetering rotor was constructed to explore aspects of flight control and stability. This was followed by a lighter second-generation prototype with a composite structure. Finally, a robust shrouded rotor vehicle incorporating a hingeless rotor was built. The conceptual design of the vehicle, experimental tests, and prototype construction are described later.

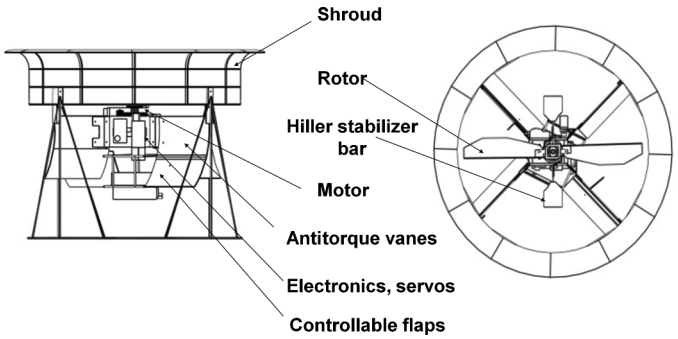

Fig. 1. TiShrov: shrouded rotor MAV design.

Vehicle Design

TiShrov is an axisymmetric vehicle that consists of a single two-bladed main rotor with fixed vanes in the downwash to counter rotor torque (Fig. 1). The rotor is hingeless, and the blades have a circular camber airfoil with sharpened leading edge. Two of the vanes have controllable flaps at the trailing edge to allow for yaw control. Some of the previously developed ducted rotor UAVs used control vanes to produce pitch and roll moments about the vehicle center of gravity. As will be shown later in this paper, the performance of these vanes deteriorates in ground effect (IGE). In addition, the requirement for an increased distance between the vane center of pressure and the vehicle center of gravity as well as extra stators for yaw stability makes the concept unattractive for implementation in an MAV. Hence, for this design, attitude control was achieved from a traditional swashplate configuration. A Hiller stabilizer bar was incorporated in the main rotor to transfer cyclic inputs to the main rotor and improve stability characteristics of the vehicle by offering passive gyroscopic feedback to the rotor. Cyclic control is achieved by attaching the Hiller bar pitch links to a commercially available swashplate actuated by two servos. Swashplate actuation is transferred to pitching of the aerodynamic paddles of the Hiller bar. Subsequent flapping of the Hiller bar results in a 1/rev cyclic input to the rotor (Fig. 2). A third servo is mechanically linked to the controllable vane flaps to deflect the flaps in a symmetric manner. A carbon fiber shroud encloses the main rotor and is integrated into the fuselage through the vanes. A brushless DC motor was chosen as the power plant to minimize the noise signature and for ease of operation. A receiver,

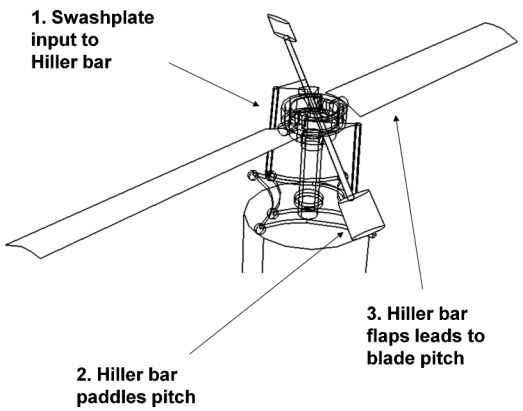

Fig. 2. Cyclic input to rotor.

speed controller and yaw gyro constitute the remainder of the on-board electronics.

Rotor blades

The rotor was designed to include two blades (for mechanical simplicity) incorporated with a Hiller stabilizer bar. The rotor for the present vehicle concept operates at low tip Reynolds (*Re*) numbers (20,000–100,000). Previous studies show that thin circular-arc cambered airfoil ($t/c < 0.05$) produced the best c_l/c_d at low *Re* numbers (Ref. 9). Experimental and computational fluid dynamics (CFD) studies on micro rotors (Refs. 10–12) indicated that the performance can be improved further by sharpening the leading edge of the airfoil. It is known (Ref. 16) that the induced losses of a full-scale rotor can be reduced by allowing for suitable twist and taper in the blades. However, previous experiments (Ref. 10) with microscale rotors did not indicate significant aerodynamic improvements due to twist. From blade design experiments, an optimum rotor design in the unshrouded configuration was chosen based on the maximum figure of merit (*FM)* achieved. The rotor had a 8–13% circular arc camber airfoil with a t/c of 2% and a sharpened leading edge. The planform had a 2:1 taper starting from 60% of the rotor radius. A maximum *FM* of about 0.64 was achieved at a blade loading (C_T/σ) of about 0.18. It must be mentioned that the identification of an optimized rotor in the unshrouded configuration is useful while evaluating and comparing the performance when a shroud encloses this rotor.

Hiller stabilizer bar

The Hiller stabilizer bar consists of aerodynamic paddles attached at each end of a teetering bar. The inertia and aerodynamic properties of the Hiller bar are such that it slows the rotor response to perturbations and improves the stability of the vehicle (Ref. 13). This is important for controllability of MAV scale vehicles. It also augments control to the rotor by transferring cyclic inputs from the swashplate to the main rotor. The radius, paddle length, and chord of the Hiller bar are 60, 30, and 27 mm, respectively. The Lock number of the rotor with the Hiller bar is 0.56. It was seen that the aerodynamic paddles of the Hiller bar consume extra power due to profile drag without significantly contributing to the total thrust. To minimize this penalty, the paddle collective was set to about 12° (about 6% drop in *FM*).

Antitorque vanes

The antitorque vane concept is one of the key design features for the prototype vehicle designs that are described in this paper. A simple analysis and a series of experimental tests were performed to study the effectiveness of these vanes at low *Re* number conditions.

For the experimental studies, a three-bladed fixed pitch rotor with a solidity of 0.15 and a diameter of 6 inches was used. The blades were rectangular in planform, untwisted, and with a circular arc airfoil section of camber 6%. The blades were set at a collective pitch of 18°. The antitorque vanes were assembled to the central body holding the DC motor driving the main rotor. Four vanes were installed, each with a chord of 3 inches. First, flat plates were used as vanes that were installed parallel to the rotor axis to study the presence of swirl in the rotor downwash. The effect on the net torque on the body was measured. Then, vanes with an 8% circular arc cross section were installed. The vanes could be set at a given pitch angle with respect to the central axis of the rotor. The amount of antitorque generated by the vanes was measured at different values of vane incidence θ_V.

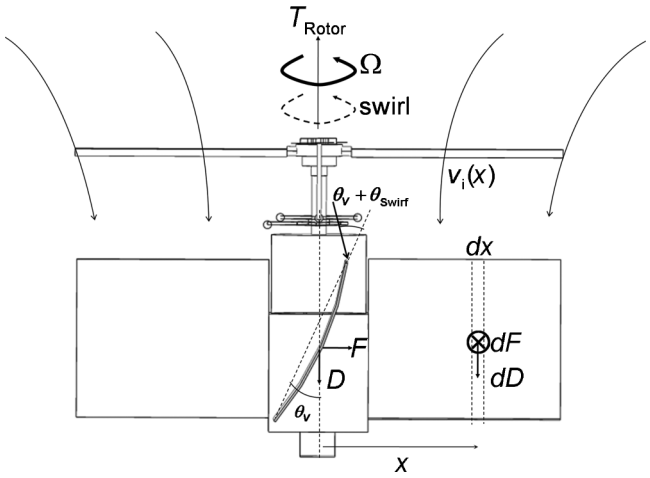

Fig. 3. Antitorque vanes: schematic.

A blade element momentum theory (BEMT) analysis was performed to estimate two important factors: antitorque capability of the vanes and the drop in net thrust due to vane down force for a given input power. The downwash encountered by the vanes is v_v such that $v_i < v_v < v_{\text{exit}}$. While BEMT requires v_v to be parallel to the rotor axis, in reality, it will include a swirl component such that the net vane angle of attack is $\theta_V + \theta_{\text{Swirl}}$. This swirl angle is estimated from flat plate vane experiments The forces F and D are the aerodynamic lift and drag generated by a single vane. A schematic is shown in Fig. 3. For the sake of analysis, the basic assumptions are (1) $v_v = 1.5v_i$, (2) area of rotor downwash influencing the vanes contracts up to about 80%, (3) the aerodynamic forces F and D perpendicular and parallel to the rotor axis, respectively, (4) Prandtl tip loss function not included, and (5) swirl angle does not change based on vane incidence and geometry. Based on these assumptions,

Rotor thrust

$$T_{\text{Rotor}} = \rho A(\Omega R)^2 C_T \tag{1}$$

Inflow velocity

$$v_i(x) = \Omega R \frac{\sigma C_{l_\alpha}}{16}\left(\sqrt{1 + \frac{32\theta_0 x}{R\sigma C_{l_\alpha}}} - 1\right), \quad \lambda_i(x) = \frac{v_i(x)}{\Omega R} \tag{2}$$

where R is the rotor radius, Ω is the rotor speed, σ is the rotor solidity, c_{l_α} is the lift curve slope around 0.05/deg for a 6% circular-arc camber airfoil, $Re = 5 \times 10^4$ (Ref. 19), and θ_0 is the blade collective (deg).

Rotor torque

$$Q_{\text{Rotor}} = \rho A(\Omega R)^2 R\left(\kappa \frac{C_T^{3/2}}{\sqrt{2}} + \sigma \frac{C_{D_R}}{8}\right) \tag{3}$$

where κ is the induced power correction factor chosen to be 1.75 for MAV scale rotors (Ref. 16), C_T is the rotor thrust coefficient, and C_{D_R} is the average drag coefficient of the rotor blade around 0.1 for a 6% camber circular camber airfoil (Ref. 19).

Vane torque

$$Q_{\text{Vanes}} = \frac{N_{\text{Vanes}}\rho v_v^2}{2}\int_0^{0.9L_V} C_{l_\alpha}(\theta_V + \theta_{\text{Swirl}})c_V x\, dx \tag{4}$$

where N_{Vanes} is the number of vanes equal to four for the present setup, $v_v$is the downwash velocity encountered by the vanes, c_{l_α} for circular-arc camber vanes is chosen to be around 0.05/deg, θ_V is the vane pitch

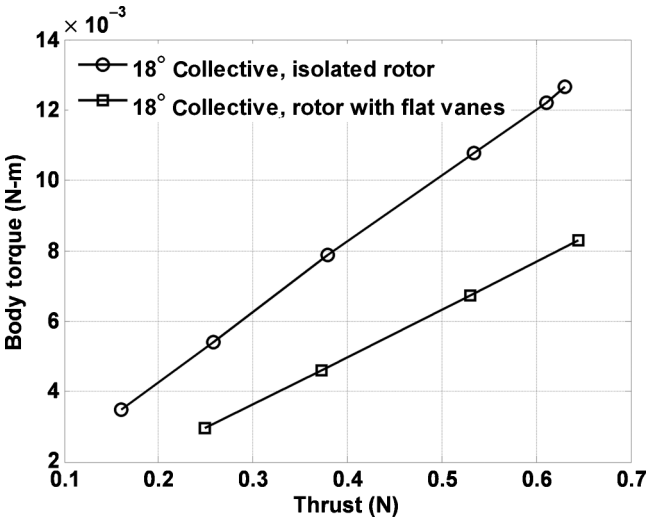

Fig. 4. Body torque vs. thrust for rotor with flat vanes at 0° inclination in rotor downwash.

setting equal to 12°, L_V is the distance between shaft axis and outer vane edge, and c_V is the vane chord.

Vane down drag

$$D_{\text{Vanes}} = \frac{N_{\text{Vanes}} \rho v_v^2}{2} \int_0^{0.9L_V} C_{D_V} c_V \, dx \tag{5}$$

where C_{D_V} is the drag coefficient for the 8% circular camber vanes, around 0.2 for an incidence angle of about 15° (Ref. 19).

Net torque (from Eqs. (3) and (4))

$$Q_{\text{Net}} = Q_{\text{Rotor}} - Q_{\text{Vanes}} \tag{6}$$

Net thrust (from Eqs. (1) and (5))

$$T = T_{\text{Rotor}} - D_{\text{Vanes}} \tag{7}$$

Input electrical power

$$P_{\text{Elec}} = \frac{Q_{\text{Rotor}} \Omega}{\eta} \tag{8}$$

where η is the motor-gearbox efficiency, chosen to be about 50% based on measured motor performance.

The experimentally measured torque on the body obtained by installing flat plates in the downwash, parallel to the axis of the rotor (0° inclination), is shown in Fig. 4. It can be seen that by just installing these flat vanes, the total torque on the body is reduced by approximately 40%. θ_V for this flat plate vane case is 0°. Using these data, the swirl angle was determined to be about 4°. This result was used to update the net vane angle of incidence and predict the effect of vanes on the net body torque (Eq. (6)) and input power (Eq. (8)) at different thrust levels (Fig. 5). It can be seen that with 8% circular camber vanes set at 12° pitch setting, a 75% torque balance was achieved. From Fig. 6, it can be seen that for a given input power, about 9% reduction in thrust was incurred due to the vane down drag.

The results of the analysis compare satisfactorily with the experimental results . The circular arc vanes at a pitch angle of 12° reduce the torque on the body by almost 80% (Fig. 5). The installation of the vanes results in an increase in power required for a given thrust by approximately 10% (Fig. 6). This percentage increase in power is similar to that typically

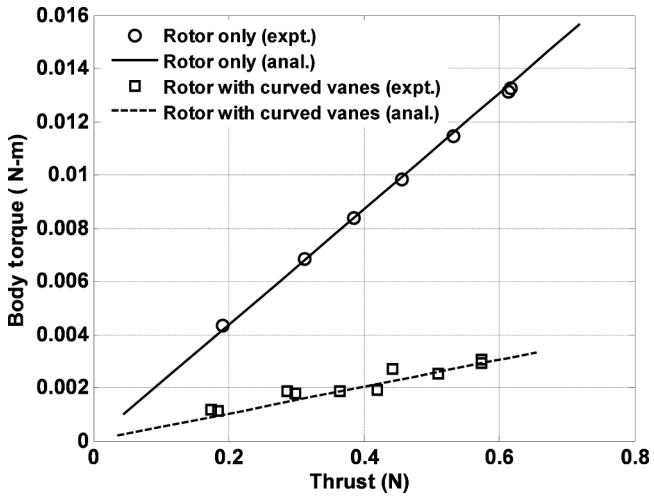

Fig. 5. Net body torque vs. thrust for curved vanes in downwash.

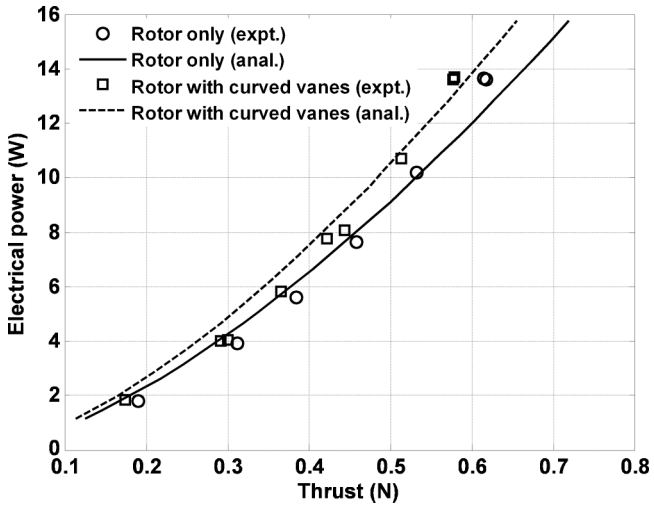

Fig. 6. Effect of vanes on power consumed.

required by a conventional full-scale tail rotor. Based on the above results, it was seen that the concept of vanes placed in the rotor downwash for countering rotor torque was viable. Hence, for the final design, two vanes were fixed and two vanes were provided with controllable trailing edge flaps for yaw control.

Hingeless hub

A hingeless rotor was chosen for the shrouded rotor configuration. The reasons for this are (1) rotor tip path plane excursions inside the shroud can lead to severe gyroscopic instabilities (Ref. 14) and (2) enhanced control power for better maneuverability and tolerance to gusts. A teetering rotor has a 90° phase lag between cyclic input and flapping response. Since the Hiller bar flapping motion provides cyclic input to the rotor, the teetering rotor and Hiller bar are placed 90° apart. With a hingeless rotor, however, this phase lag is less than 90°. If the Hiller bar and the rotor are not correctly phased, a gust disturbance or fuselage attitude perturbation can cause cross-coupling in pitch and roll attitude of the vehicle (Ref. 15). This is detrimental to stability of the vehicle.

Therefore, a hub was designed with circular slots to allow for adjustments in the Hiller bar phasing as can be seen from Fig. 7. Since the

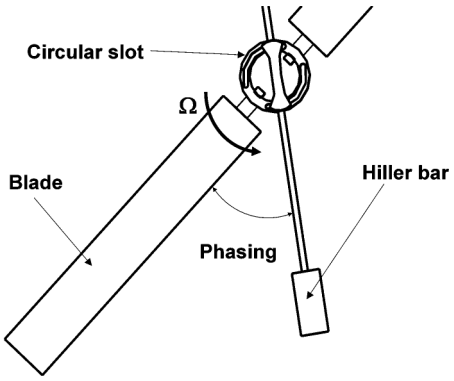

Fig. 7. Hingeless hub: phased Hiller bar.

stiffness of the rotor blade was not exactly known, it was necessary to determine the desired phase angle between the Hiller bar and the main rotor.

Theoretical method. The phase lag between the cyclic input and rotor response is given by

$$\phi = \tan^{-1}\left(\frac{\gamma_R}{\nu_\beta^2 - 1}\right) \tag{9}$$

where ν_β is the nondimensional rotating natural flap frequency of the rotor blade and γ_R the Lock number of the rotor. For a teetering rotor case, the phasing is exactly 90° ($\nu_\beta = 1$). For a hingeless rotor, it can be shown that the phasing is ϕ (Eq. (9)). The phasing was determined by obtaining ν_β from a measurement of the nondimensional nonrotating flap frequency $\nu_{\beta_{\mathrm{NR}}}$. The operating rpm was set at 3,000. The flap frequency was measured from the blade impulse response.

Experimental method. The phase angle of the Hiller bar was then experimentally validated. The rotor system was attached to a shaft that was connected to a torque load cell at the other end. Cyclic input was given such that the torque cell measured the off-axis moment. The Hiller bar was manually adjusted over a range of angles for each rotor speed. At each rpm, the desired phasing angle was determined as the angle when zero off-axis moment occurred. Figure 8 shows the variation of the desired phasing angle Ψ_{C_0} as a function of operating rpm. It can be seen that Ψ_{C_0} increased with operating rpm since ν_β decreased. Overall, there was a good agreement between the predicted and measured phase angles. For

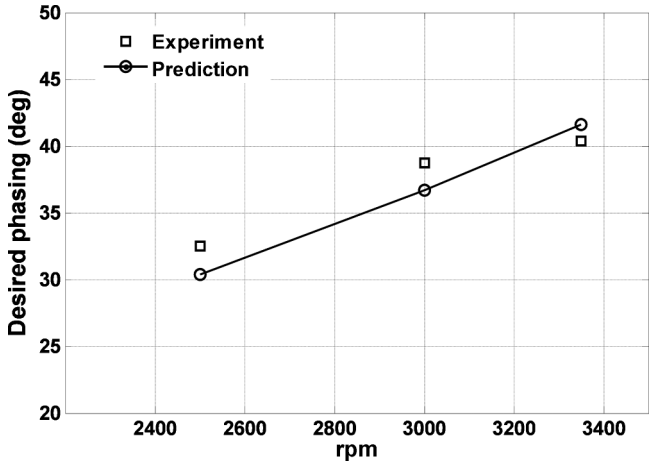

Fig. 8. Variation of desired phasing with rpm.

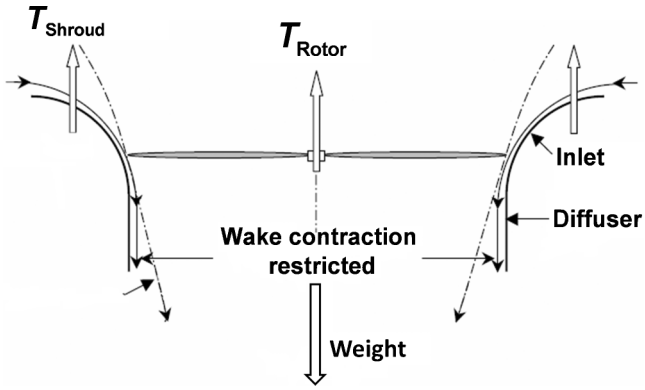

Fig. 9. Division of thrust: rotor and shroud.

an operating rpm of 3,000, the Hiller bar was set to be leading the blade by about 40°.

Shroud

In addition to blade optimization, the hover efficiency of an MAV can be enhanced by enclosing the rotor in a shroud. Unlike a conventional rotor, the thrust of a shrouded rotor includes two parts, the thrust of the rotor and the additional thrust of the shroud. The additional benefit is enhanced rotor protection offered by the shroud.

The two sections considered for a shroud design are inlet and diffuser (Fig. 9). The diffuser recovers kinetic energy of the slipstream and increases the mass flow rate through the rotor (for the same total thrust produced by the shrouded rotor and an isolated rotor). Airflow over the inlet surface creates a suction force which results in a lift force. Let T_{Total} be the total thrust of the shrouded rotor, T_{Isolated} be the thrust generated by an isolated rotor of the same disk area, and σ_d be the wake contraction ratio (greater than 1 for an expanding diffuser section). When compared at same induced power, it can be shown from simple momentum theory that (Ref. 16)

$$\frac{T_{\mathrm{Total}}}{T_{\mathrm{Isolated}}} = (2\sigma_d)^{1/3} \tag{10}$$

For a straight diffuser section, this thrust ratio is 1.26. It is assumed that the flow expands to atmospheric pressure at the diffuser exit. In reality, this number is lower due to losses that may be attributed to tip losses (Ref. 18), duct skin friction, slipstream rotation, and flow separation over the inlet and/or diffuser. In a recent study (Ref. 17), an optimum combination of design parameters (Fig. 10) for an MAV-scale shrouded rotor was identified to minimize these losses. Key conclusions from this study relevant to the present design were (1) a blade tip clearance ($\delta_{\mathrm{tip}} < 0.012R$) needs to be maintained for good performance, (2) the diffuser angle (θ_d) plays a more important role than the diffuser length (L), and (3) the outer portion of the shroud lip does not play a major role in thrust production. Hence, for weight savings, the lip chord can be shortened.

It can be seen that for this concept to be viable, the thrust improvement offered by a shrouded rotor for a given operating power should be at least greater than the weight of the shroud itself. A design analysis based on simple momentum theory to estimate the upper limit for the shroud mass is described below.

Let W_{US} be the weight of the unshrouded MAV, W_{Shroud} the weight of the shroud, and W_S the weight of the shrouded MAV. Consequently,

$$W_S = W_{\mathrm{Shroud}} + W_{\mathrm{US}} \tag{11}$$

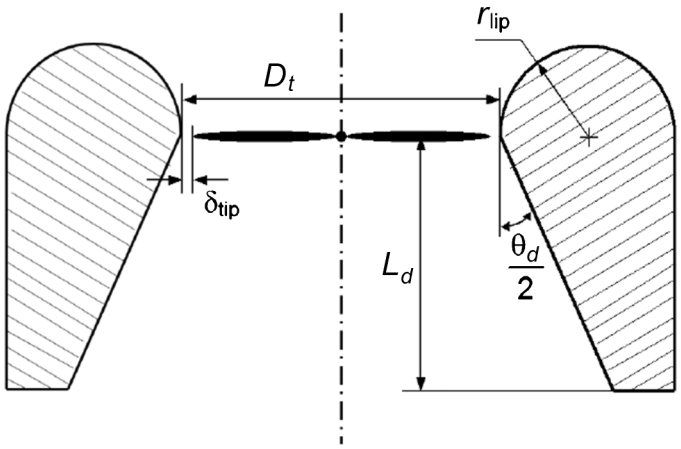

Fig. 10. Shroud design parameters.

The mechanical power consumed by any rotor can be written as

$$P = P_P + P_I \tag{12}$$

The profile power (P_P) is mainly a function of the rotor solidity and airfoil drag coefficient. The induced power (P_I), however, depends on the structure of the wake. Since the rotor configuration is fixed, it can be logically assumed that the main differences in mechanical power consumption between an unshrouded and shrouded rotor are from the induced power. Therefore, for a useful shroud design,

$$P_{I_S} < P_{I_{\text{US}}} \tag{13}$$

In nondimensional terms,

$$C_{P_{I_S}} < C_{P_{I_{\text{US}}}} \tag{14}$$

From simple momentum theory, for a given contraction ratio σ_D, the nondimensional induced power is given by

$$C_{P_I} = \kappa \frac{(W)^{3/2}}{\sqrt{(4\sigma_D \rho A)}} \tag{15}$$

where κ is the induced power factor that accounts for tip loss effects, nonuniform inflow, and swirl effects. W is the weight of the vehicle, A is the area of the rotor disk, which is maintained constant, and ρ the air density. Hence, for

$$C_{P_{I_S}} < C_{P_{I_{\text{US}}}} \tag{16}$$

$$\kappa_S \frac{(W_S)^{3/2}}{\sqrt{(4\sigma_D \rho A)}} < \kappa_{\text{US}} \frac{(W_{\text{US}})^{3/2}}{\sqrt{(2\rho A)}} \tag{17}$$

This leads to

$$\frac{W_S}{W_{\text{US}}} < \left(\frac{\kappa_{\text{US}}}{\kappa_S}\right)^{2/3} (2\sigma_D)^{1/3} \tag{18}$$

Since the shroud diffuses the rotor tip vortex (Ref. 18), the induced losses from a shrouded rotor are expected to be lower than an isolated rotor. Consequently, $\kappa_{\text{US}} > \kappa_S$. A conservative estimate for the weight restriction for the shroud can be made by assuming $\kappa_{\text{US}} \sim \kappa_S$. Hence, from Eqs. (11) and (17),

$$W_{\text{Shroud}} < \left((2\sigma_D)^{1/3} - 1\right) W_{\text{US}} \tag{19}$$

For example, if the weight of the unshrouded vehicle is 250 g, and if $\sigma_D = 1$, the power loading of the vehicle can be improved by enclosing the rotor in a shroud weighing less than 65 g.

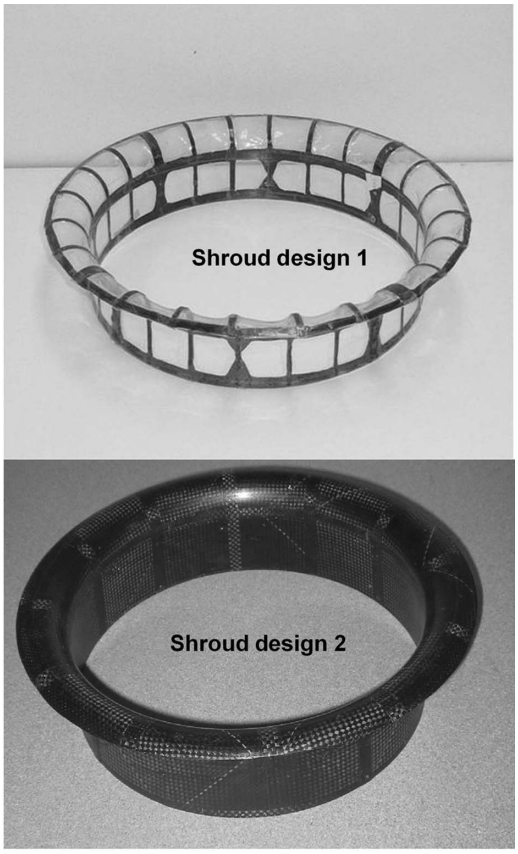

Fig. 11. Shroud designs.

However, due to the shroud lip, the dimension of a shrouded rotor MAV in the rotor plane is equal to an isolated rotor MAV with a larger rotor diameter. To accommodate the effect of the increased size, the revised restriction for the shroud weight becomes

$$W_{\text{Shroud}} < \left(\left(2\frac{A}{A'\sigma_D}\right)^{1/3} - 1\right) W_{\text{US}} \tag{20}$$

where A is the area of the rotor disk and A' is the area of the shroud including the shroud lip. Consider the previous example of a 250-g unshrouded rotor MAV with an 11-inch diameter rotor. For the same dimension, the shrouded rotor MAV should consist of an 11-inch diameter shroud. If the diameter of the rotor is 9 inches, for power loading improvements, the weight of the shroud should not exceed 25 g.

These weight restrictions pose challenges for shroud construction that include (1) lightweight material construction without compromising on shroud stiffness and (2) uniform surface construction to ensure uniformity in pressure distribution over shroud inlet. Shroud construction iterations were carried out based on two designs to determine a stiff, lightweight structure.

Shroud design 1. A shroud structural frame was constructed out of 1–2-mm-thick strips made from cured carbon/epoxy that were suitably arranged to stiffen the structure in torsion and in the radial direction. The frame was covered with clear cellophane tape. The design is shown in Fig. 11. The shroud weighed 41 g. For this design, $r_{\text{lip}} = 9\% D_t$, $L = 15\% D_t$, and $\sigma_D = 1$. The diffuser length was restricted to save weight and minimize surface friction losses.

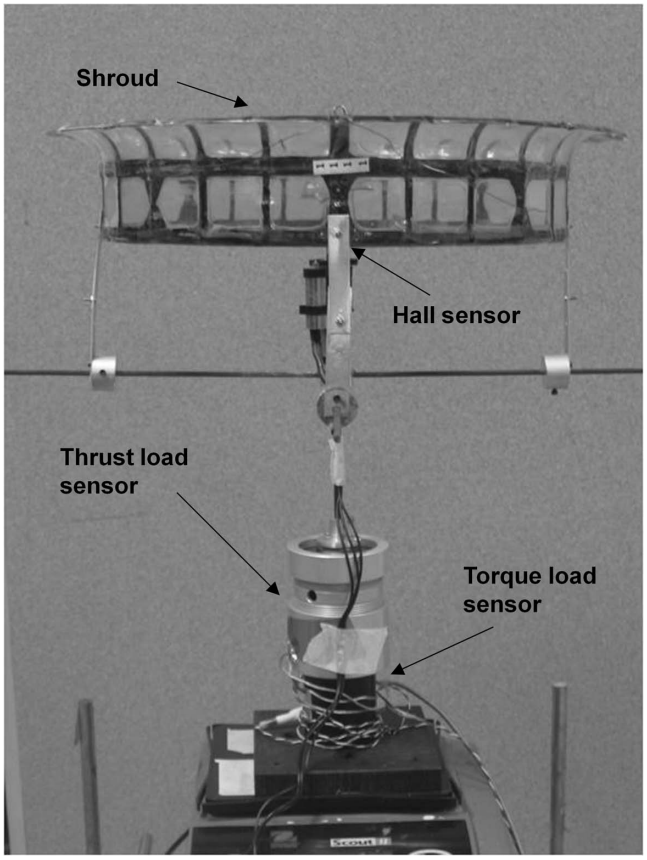

Fig. 12. Shrouded rotor hover test stand.

Shroud design 2. This design consisted of a single ply of carbon fiber/epoxy weave on a framework of unidirectional graphite epoxy stiffeners. The shroud was constructed by laying up the plies in a female metal mold, vacuum bagging, and curing in an oven (Fig. 11). A chord-diameter ratio of 0.5 was chosen to save weight. The shroud weighed about 45 g. Shroud design 1 was stiffer in the radial and out-of-plane torsion mode as compared to shroud design 2, whereas the second design had a uniform shroud inlet surface. However, a stiffer shroud was preferred to avoid undesirable rotor shroud interference. Hence, results of the performance tests discussed here are with shroud design 1.

To estimate the aerodynamic performance of the shroud, the shrouded rotor was tested on the micro rotor hover stand (Fig. 12). A central member with four arms that held the shroud was rigidly attached to the shaft. This allowed the measurement of the total thrust of the shrouded rotor for a given mechanical power input. For comparison, the optimum rotor in the unshrouded configuration mentioned previously was used. The shrouded rotor was tested with the shroud enclosing this rotor. The tip clearance was set to about $0.015R$, since lower tip clearances resulted in rotor–shroud interference. To study the individual contribution to the total thrust from the rotor and the shroud, a modified thrust stand was constructed. For this, two load cells were used. The first load cell measured the rotor thrust while the second measured the total thrust. The difference in these two measurements is the thrust due to the suction on the shroud inlet surface. It should be mentioned that since the rotor shaft was not directly attached to the shroud, any vibration in the shaft resulted in rotor–shroud interference. To avoid this, a higher tip clearance of about $0.03R$ was used.

Figure 13 compares the most efficient performance obtained for the shrouded and unshrouded rotor. It can be clearly seen that the shrouded

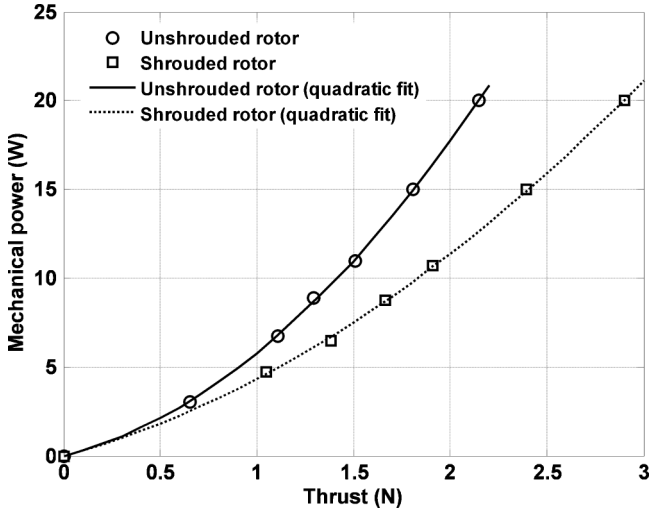

Fig. 13. Power thrust comparision between shrouded and isolated rotor.

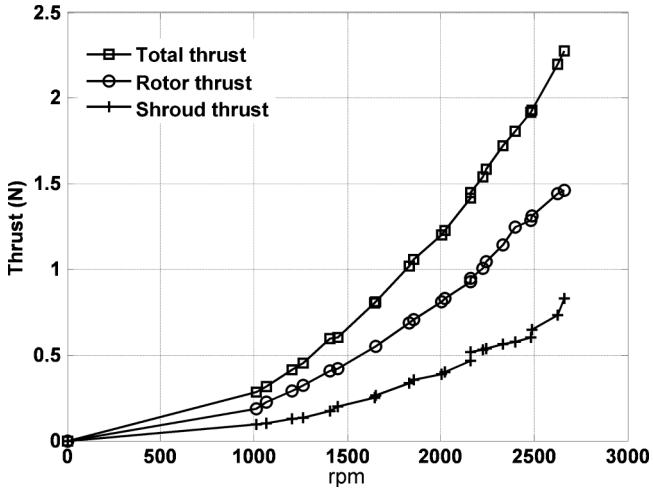

Fig. 14. Thrust contribution from rotor and shroud.

rotor has a better aerodynamic performance than the unshrouded rotor. For example, for an input mechanical power of 15 W, the improvement in shrouded rotor thrust is about 70 g. This clearly exceeds the weight of the shroud, thus leading to a payload benefit of about 30 g.

Figure 14 shows a representative result for $T_{\text{Shroud}}/T_{\text{Total}}$ for the rotor operated at 26° collective. It can be seen that the rotor shared a higher proportion of the total thrust compared to the shroud. The ratio of the shroud thrust to the total thrust is between 0.3 and 0.4, which is below the ideal momentum theory estimate of 0.5. This is expected due to tip loss effects and diffuser wall skin friction drag. Based on the above results, it was seen that the shroud design was effective in improving the vehicle power loading.

Flight Testing

A series of risk reduction prototypes (Table 2) were constructed and flight tested prior to the final shrouded rotor vehicle testing.

Table 3. Vehicles: weight breakdown

	Prototype					
	TiFlyer		Giant		TiShrov	
Component	Mass (g)	Percentage of Total	Mass (g)	Percentage of Total	Mass (g)	Percentage of Total
Rotor system	30.5	8.9	18.3	7.6	25	9.7
Swashplate	20	5.8	8.1	3.4	12	4.7
Battery	106.2	30.9	53.3	22.2	53.3	20.7
Motor	52.7	15.3	52.7	22	16.9	6.6
Electronics and servos	38	11	38	15.9	38	14.8
Structure	96.5	28.1	69.2	28.9	112	43.5
Total	343.9	100	239.6	100	257	100

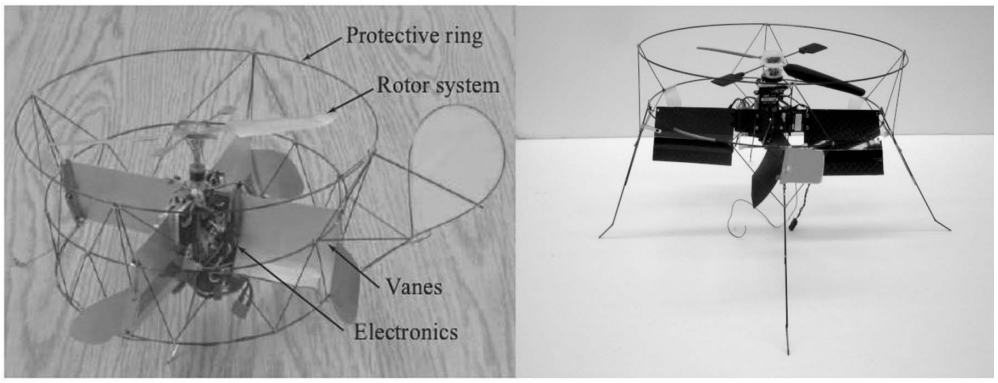

(a) TiFlyer (b) Giant

Fig. 15. Vehicle prototypes.

TiFlyer

The main goal of this prototype was to demonstrate the antitorque vane concept in flight. It was constructed as shown in Fig. 15(a). A two-bladed aluminum sheet teetering rotor was incorporated along with a Hiller stabilizer bar. The rotor had a diameter of 250 mm and a blade solidity of 0.129. Lateral and longitudinal control was achieved through actuating cyclic input to the Hiller bar. A lightweight carbon fiber frame was installed to protect the rotor and to add stiffness to the body. The vanes were made of curved metal sheets and were held to the center body through metal connector plates. Two of the vanes were provided with controllable surfaces which were actuated by a single servo in a symmetric manner. The weight breakdown of the vehicle is given in Table 3. TiFlyer exhibited stable hover characteristics and satisfactory maneuverability during flight testing.

Giant

The next prototype was built with the main goal of minimizing the vehicle weight (Fig. 15(b)). The aluminum sheet blades were replaced with carbon/epoxy blades. This decreased the blade weight from 4.2 to 2.6 g. As a result, it was possible to construct the hub from a lighter material (Delrin). Thin sheet carbon fiber vanes were held to the center body through connecter plates and to the outer carbon fiber frame. A spider-type swashplate was incorporated as shown in Fig. 16. Here, the swashplate motion occurs in the plane of the rotor, in contrast to a conventional swashplate. The two servos move the nonrotating part in two orthogonal directions. The rotating part is attached to the nonrotating part by a radial bearing, and the result of the servo motion is an eccentricity of the center of rotation of the rotating part with respect to the main rotor shaft. This eccentricity is used to transfer a cyclic pitch angle to the servo-paddle by means of a control linkage sliding in a slot in the rotating part of the swashplate. This reduced the number of moving parts and the mechanical integrity of the actuation system was improved. The electronics, battery, and motor remained unchanged from that of TiFlyer. The weight breakdown of Giant is given in Table 3. It can be seen that a structural weight reduction was achieved by using composites.

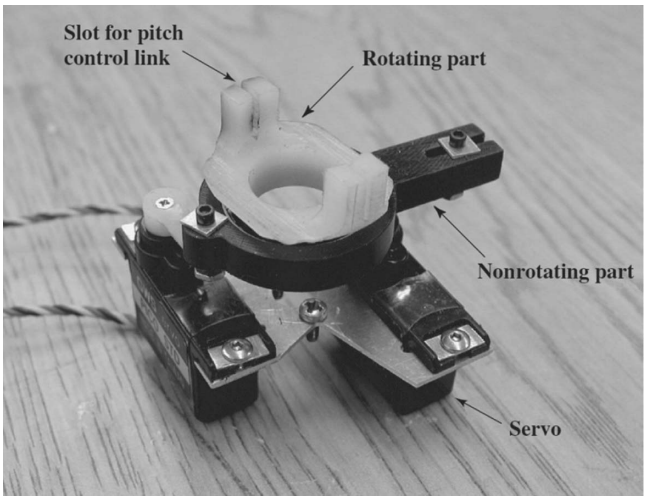

Fig. 16. Spider swashplate.

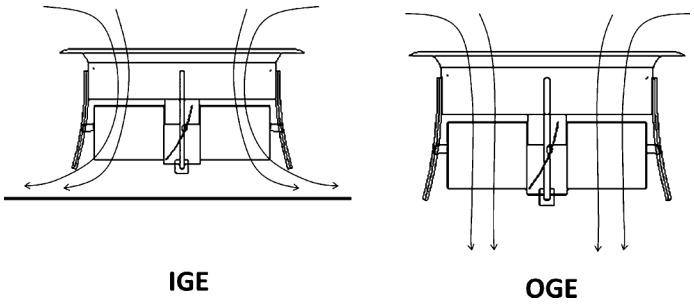

Fig. 17. Loss of vane effectiveness IGE.

Giant also exhibited good hover and maneuverability during flight testing. Based on observation and pilot feedback, it was noticed that the yaw authority offered by vanes was lower than a conventional tail rotor. Another observation was the reduced antitorque capability of the vanes when operated IGE. Tests were performed to study this phenomenon.

Effect of ground on vane effectiveness

A possible explanation for the deteriorated yaw control authority IGE is illustrated in Fig. 17. With ground proximity, the pressure in the center of the rotor downwash increases. This has two effects: (1) inflow velocity through the rotor decreases and (2) the rotor downwash is pushed radially outward. A combination of these factors is probably responsible for the degradation in vane effectiveness IGE. This effect was studied through unconstrained (string suspension) and constrained (Fig. 18) setups. TiShrov was used for these studies since the presence of the hingeless rotor and shroud was favorable for performing string suspension studies.

Unconstrained setup to study vehicle yaw authority. The vehicle was suspended by a string fixed to a carbon rod that was attached to the shroud structure. The height of the vehicle above the ground was varied from IGE to OGE (out of ground effect) condition. The inertial measurement unit (IMU) yaw rate data (via Bluetooth) and rudder–throttle input from the transmitter (via a microcontroller) were recorded. The yaw rate response of the vehicle as a function of height is shown in Fig. 19. Also shown are the pilot throttle and rudder stick inputs. Extra weight was added to the vehicle to prevent string slackening. The rudder input was symmetrically swept about the mean position in clockwise and anticlockwise rotation. The rotor was spun in the anticlockwise direction (looking from top). As expected, a significant difference in vehicle yaw response was observed between IGE (Fig. 19(a)) and OGE (Fig. 19(b)) conditions. With maximum control deflection, the vanes were not able to counter the rotor torque IGE (height above ground $z/R = 1.3$). It was seen that yaw authority improved as the vehicle came OGE. A maximum yaw rate of about 1.8–2 rad/s was attainable.

Constrained setup to study yaw authority. Maximum obtainable body torque from vane deflections was measured as a function of height above ground. From Fig. 20, it can be observed that in OGE condition, the vehicle trimmed in yaw. This implied equal control authority in clockwise and counterclockwise directions. Such was not the case when the vehicle operated closer to the ground. It can be seen that for a fixed vane and undeflected control vane setting of 23° and 16°, respectively, equal bidirectional yaw authority was achieved in OGE condition (Fig. 21). However, for the IGE condition, the vane angles had to be increased. Thus for a given vane setting similar yaw authority cannot be achieved in IGE and OGE conditions.

Based on the above study, the vane pitch setting was appropriately varied depending on the region of operation (IGE or OGE).

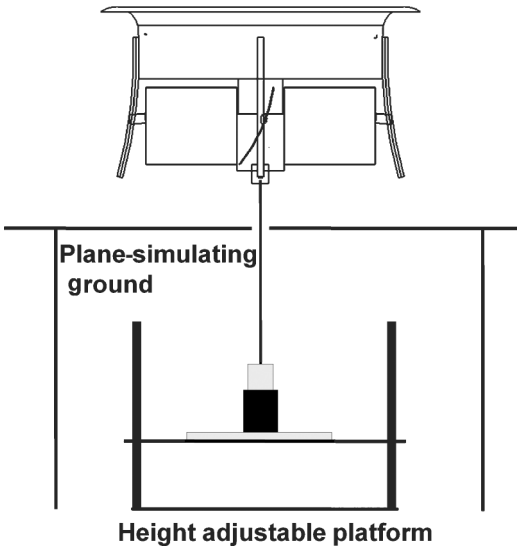

Fig. 18. Setup to measure effect of ground on vane effectiveness: constrained in yaw.

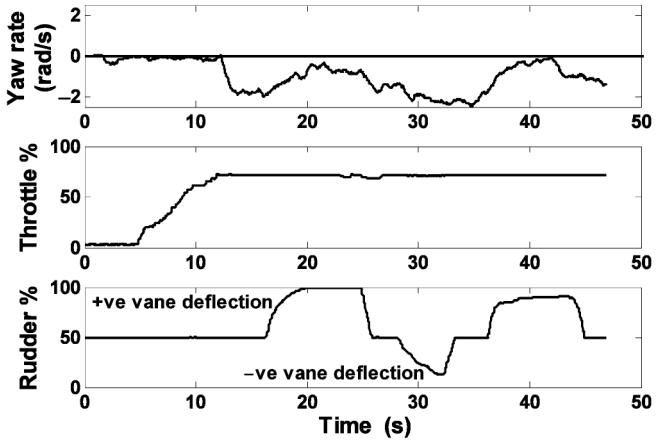

(a)

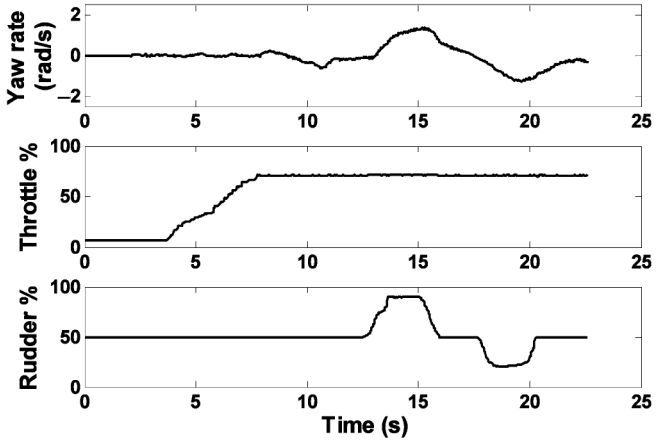

(b)

Fig. 19. (a) $z/R = 1.3$, unconstrained IGE; and (b) $z/r = 2.5$, unconstrained OGE.

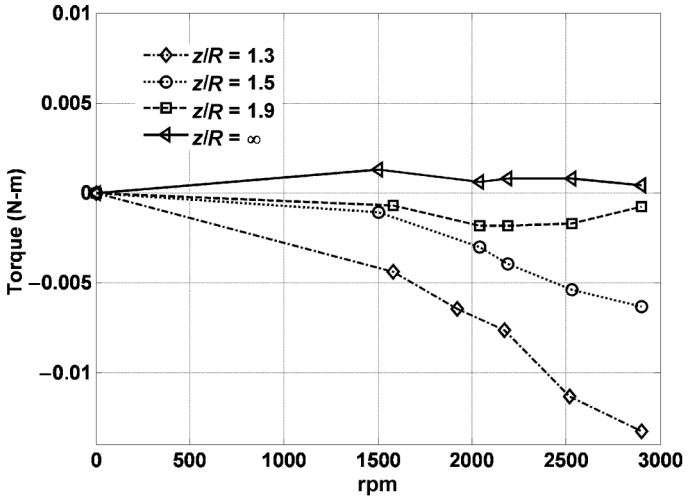

(a) Vanes undeflected

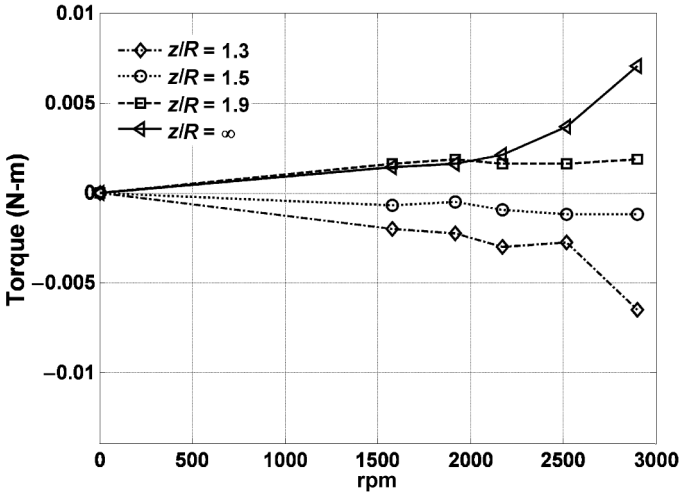

(b) Vanes deflected

Fig. 20. Loss of vane effectiveness as vehicle approaches ground.

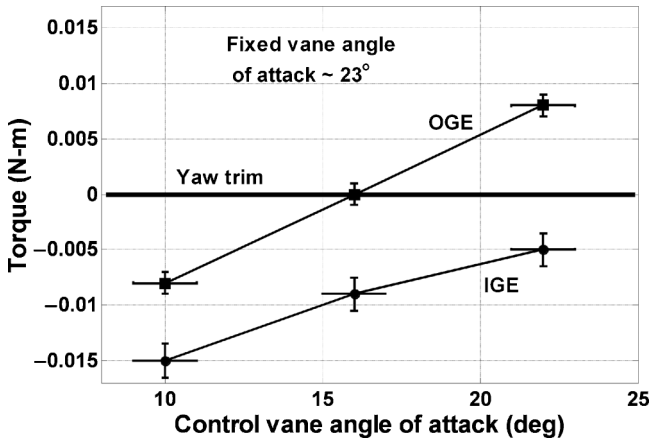

Fig. 21. Bidirectional yaw authority IGE and OGE.

TiShrov

A third prototype vehicle to demonstrate the shrouded rotor concept was constructed as shown in Fig. 22(a). It can be seen that apart from the shroud, the key difference between Giant and TiShrov is the choice of a hingeless rotor. The Hiller bar was phased at about 40° to the blade pitching axis to minimize cross-coupling between control input and rotor response. The phased Hiller bar-rotor was driven by a 55 W DC brushless in-runner motor with an 8:1 gearbox. A commercially available swashplate was used to transfer inputs from two micro servos to the phased Hiller bar for pitch and roll control. The yaw control surfaces were actuated in a manner similar to TiFlyer and Giant. The motor and gearbox were enclosed in an aluminum central body to which the vanes, electronics, and servos were attached. The weight breakdown of the vehicle is shown in Table 3.

The Hingeless rotor of TiShrov resulted in a much faster rotor response making it extremely difficult for a human pilot to control. An onboard stability augmentation system was developed based on a closed-loop proportional–integral–derivative (PID) controller (Ref. 14). An IMU was mounted on the shaft axis of the vehicle. It consisted of three gyros and one triaxial accelerometer. A suitable complementary filter was applied to the output of these sensors to provide vehicle attitude measurement. A proportional feedback control was setup to minimize any disturbances in the vehicle attitude from hover condition. However, the vehicle instabilities were excessive and could not be controlled with closed-loop feedback. It was thought that since shroud design 1 (Fig. 11) did not have a uniform surface, the azimuthal distribution of suction forces would not be uniform and hence unstable moments would be transferred to the fuselage. Therefore, shroud design 2 (Fig. 11) was incorporated due to its smooth inlet surface. The modified shrouded rotor vehicle TiShrov-2 is shown in Fig. 22(b). TiShrov-2 was successfully flown in hover using PID control (Ref. 14).

Conclusions

The design and testing of a shrouded single-rotor MAV with antitorque vanes exhibiting improved hover efficiency is described. The final vehicle weighs 257 g and consists of a two-bladed single hingeless rotor of diameter 240 mm enclosed in a shroud. The shroud is attached to axisymmetric vanes that are placed in the rotor downwash to provide antitorque. Bench top tests were conducted to evaluate the performance of the shrouded rotor and antitorque system.

(1) This vehicle design proposes improved efficiency by enclosing the rotor in a shroud. The rotor operates at low tip Reynolds number (20,000–100,000). For power loading improvement over an unshrouded rotor MAV, a simple momentum theory based design analysis suggested that for a shroud with a straight diffuser section, its weight should not exceed about 26% of the weight of the unshrouded vehicle. It was found that the shroud shared about 30–40% of the total thrust produced by the shrouded rotor. At an operating thrust of 2.45 N, a 40% improvement in power loading was observed, which translates to about 30-g increase in payload for a given input power.

(2) A Hiller stabilizer bar was incorporated in the rotor to improve vehicle stability and control. However, the circular bar cross-section and paddles of the Hiller bar lead to additional losses due to profile drag. It was found that by adjusting the Hiller paddle collective to about 12°, it was possible to minimize the profile losses.

(3) A hingeless rotor was incorporated to minimize the tip path plane motion in the shroud. The Hiller bar was optimally phased with the blade pitching axis to eliminate possible cross-coupling in pitch and roll due to gust disturbance and fuselage attitude perturbations. At an operating rpm of 3,000, the Hiller bar and the main rotor were set at 40° apart. It was also observed that as the operating rpm increased, the phasing increased.

(4) Performance tests suggested that vanes placed in the rotor downwash sufficiently countered the rotor torque and was independent of the

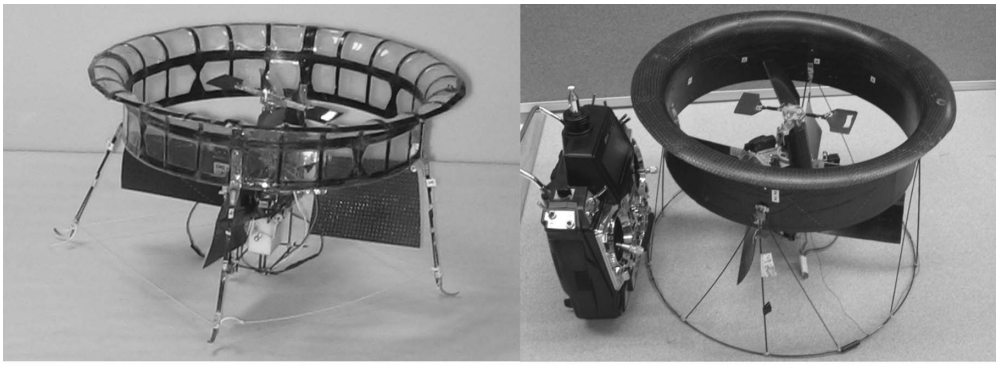

(a) TiShrov-1 (b) TiShrov-2

Fig. 22. TiShrov: shrouded rotor MAV.

operating thrust. For a given input electrical power, the thrust penalty of installing the antitorque vanes was less than 10%. However, there is a degradation in vane performance when operated IGE due to the modified structure of the rotor wake.

(5) A series of risk reduction prototypes were constructed to finally demonstrate flight capability of the shrouded rotor. Two prototype vehicles with a single main rotor and turning vanes were built. The first prototype TiFlyer constructed out of aluminum sheet weighed about 340 g. The second prototype Giant was predominantly fabricated out of carbon fiber and has a total mass of 240 g. Both prototypes were test flown and demonstrated stable lateral and yaw characteristics. The final vehicle with the shrouded rotor, TiShrov, was developed and test flown. A PID controller was used to attain stable hover since this configuration had poor inherent stability.

Future work involves characterizing the forward-flight and gust response of the vehicle.

Acknowledgments

This investigation was conducted under Multidisciplinary University Research Initiative (MURI) grant W911NF0410176 from the Army Research Office, with Mr. Tom Doligalski as Technical Monitor. The assistance of Shane Boyer and Ben Hance for flight testing tasks is greatly appreciated.

References

[1]Sacks, A., and Burnell, J., "Ducted Propellers—A Critical Review of the State of the Art," *Progress in Aeronautical Sciences,* Vol. 3, 1962, pp. 85–135.

[2]Mouille, R., "The 'Fenestron' Shrouded Tail Rotor of the SA 341 Gazelle," *Journal of the American Helicopter Society*, Vol. 15, (4), October 2007, pp. 31–37.

[3]Walsh, D., and Cycon, J. P., "The Sikorsky Cypher UAV: A Multi-Purpose Platform with Demonstrated Mission Flexibility," American Helicopter Society 54th Annual Forum Proceedings, Washington, DC, May 20–22, 1998.

[4]Mraz, S. J., *Machine Design,* Penton Media Publication, New York, NY, December 9, 2009, p. 48.

[5]Lipera, L., Colbourne, J. D., Tischler, M. B., Hossein Mansur, M., Rotkowitz, M. C., and Patangui, P., "The Micro Craft ISTAR Micro-Air Vehicle: Control System Design and Testing," American Helicopter Society 57th Annual Forum Proceedings,Washington, DC, May 9–11, 2001.

[6]Johnson, E., and Turbe, M., "Modeling, Control and Flight Testing of a Small Ducted Fan Aircraft," AIAA Guidance, Navigation, and Control Conference and Exhibit, San Francisco, CA, August 15–18, 2005.

[7]Kay, A. L, and Smith, J. R., *German Aircraft of the Second World War*, U.S. Naval Institute Press, Annapolis, MD, 2002, pp. 295–296.

[8]Sirohi, J., Tishchenko, M., and Chopra, I., "Design and Testing of a Micro-Aerial Vehicle with a Single Rotor and Turning Vanes," American Helicopter Society 61st Annual Forum Proceedings, Grapevine, TX, June 1–3, 2005.

[9]Mueller, T. J., *Fixed and Flapping Wing Aerodynamics for Micro Air Vehicle Applications,* AIAA, Reston, VA, 2001, Chap. 3.

[10]Bohorquez, F., Pines, D., and Samuel, P., "Small Rotor Design Optimization Using Blade Element Momentum Theory and Hover Tests," *Journal of Aircraft,* Vol. 47, (1), 2010, pp. 268–283.

[11]Hein, B., and Chopra, I., "Hover Performance of a Micro Air Vehicle: Rotors at Low Reynolds Number," *Journal of the American Helicopter Society,* Vol. 52, (3), July 2007, pp. 254–262.

[12]Lakshminarayan, V., and Baeder J., "Computational Investigation of Microscale Coaxial-Rotor Aerodynamics in Hover," *Journal of Aircraft,* Vol. 47, (3), 2010, pp. 940–955.

[13]Mettler, B., *Identification, Modeling and Characteristics of Miniature Rotorcraft*, Springer, New York, NY, 2002, Chap. 3.

[14]Hrishikeshavan, V., and Chopra, I., "Development of Closed Loop Flight Control for a Shrouded Rotor Micro Air Vehicle with Anti-Torque Vanes," American Helicopter Society International Specialists' Meeting on Unmanned Rotorcraft, Scottsdale, AZ, January 20–22, 2009.

[15]Hrishikeshavan, V., Sirohi, J., Tishchenko, M., and Chopra, I., "Design and Stability of a Shrouded Rotor Micro Air Vehicle with Anti-Torque Vanes," American Helicopter Society International Specialists' Meeting on Unmanned Rotorcraft, Chandler, AZ, January 23–25, 2007.

[16]Leishman, J. G., *Principles of Helicopter Aerodynamics* , Cambridge University Press, New York, NY, 2000, Chap. 6.

[17]Pereira, J. L., and Chopra, I., "Hover Tests of Micro Aerial Vehicle–Scale Shrouded Rotors, Part I: Performance Characteristics," *Journal of the American Helicopter Society*, **54**, 012001, 2009.

[18]Goodman, T. R., "The Tip Correction for Wind-Tunnel Tests of Propellers," *Journal of the Aeronautical Sciences*, Vol. 23, (12), December 1956, pp. 1094–1098.

[19]Null, W., and Shkarayev, S., "Effect of Camber on the Aerodynamics of Adaptive-Wing Micro Air Vehicles," *Journal of Aircraft,* Vol. 42, (6), 2005, pp. 1543–1547.